The phase diagram and electronic structure of Pd-V alloys: *ab initio* density functional calculations

2001 J. Phys.: Condens. Matter 13 3545

(http://iopscience.iop.org/0953-8984/13/14/324)

INSTITUTE OF PHYSICS PUBLISHING JOURNAL OF PHYSICS: CONDENSED MATTER

J. Phys.: Condens. Matter **13** (2001) 3545–3572 www.iop.org/Journals/cm PII: S0953-8984(01)20423-8

The phase diagram and electronic structure of Pd–V alloys: *ab initio* density functional calculations

Robin Hirschl, Jürgen Hafner and Yannick Jeanvoine[1]

Institut für Materialphysik and Centre for Computational Materials Science, Universität Wien, Sensengasse 8/12, A-1090 Wien, Austria

Received 4 January 2001, in final form 31 January 2001

Abstract

A parameter-free approach based on *ab initio* density functional calculations is shown to describe the phase stability and order–disorder transformations in Pd–V substitutional alloys and intermetallic compounds with remarkable accuracy, allowing first-principles calculations of the complete alloy phase diagram. The investigations are based on electronic structure and total-energy calculations for ordered compounds and disordered alloys (treated in a supercell approximation) using gradient-corrected exchange–correlation functionals and a plane-wave-based all-electron method. All calculations involve a complete optimization of all structural degrees of freedom. The calculation of the free energies of the competing phases is based on rather simple mean-field descriptions of long- and short-range-ordering phenomena, using concentration-dependent interchange and shell interaction parameters. In addition, the electronic structures of ordered compounds and of substitutional alloys have been analysed.

1. Introduction

The ability to predict the structure of metallic alloys and the physico-chemical properties of the stable phases as a function of composition and temperature is of considerable scientific and technological interest. The first step is to determine the ground states, i.e. the stable phases at zero temperature, as a function of composition by performing a series of *ab initio* total-energy calculations for a those structures that are suspected of being ground states or excited states with a small energy difference with respect to the ground state. Evidently, the success depends critically on the ability to guess the correct minimum-energy structures. The problem is considerably simplified if the search is restricted to those intermetallic structures which can be considered as superstructures of the common structures of the pure metallic elements, i.e. either fcc, bcc or hcp. In such a case the problem of enumerating the possible low-energy superstructures is much easier and can, in favourable cases, even be solved exactly. The approach commonly used is to project the problem on a three-dimensional 'Ising-like' Hamiltonian and expand the internal energy in terms of composition-independent 'effective

[1] Present address: Université d'Evry Val d'Essonne, Boulevard F Mitterand, F-91025 Evry Cédex, France.

0953-8984/01/143545+28$30.00

cluster interactions' (ECIs) [1, 2]. The ECIs have been treated in the past as empirical adjustable parameters, and global searches for ground states for all possible choices of the ECIs have been performed [3, 4]. Nowadays, the ECIs may be derived from *ab initio* total-energy calculations for selected model structures and used for obtaining the ground states for a specific alloy system [5–7]. The second step in a phase diagram calculation consists in using the ECIs to calculate the configurational entropy of possible disordered phases using a statistical-mechanical approach such as the mean-field approximation, the cluster-variation method or Monte Carlo simulations to determine the free energies of the competing phases (adding, as far as necessary, vibrational and electronic contributions) and finally the coexistence lines in the composition–temperature phase diagram. The problem with such an approach is that complex electron-mediated interactions are mapped onto a classical Hamiltonian and that there is no guarantee that this mapping is unique or rapidly convergent. Since parameters are extracted from calculations on systems with small unit cells, it is possible that the interactions contain terms favouring such structures over the disordered phases. The general tendency to overestimate the critical temperatures for ordering transitions seems to confirm this suspicion.

The approach based on ECIs starts from the ordered intermetallic compounds and uses the information on the effective interatomic interactions to estimate the energetics of the disordered phases. An alternative approach is to start from a model of the disordered alloys, treated in some effective-Hamiltonian approximation such as the coherent potential approximation (CPA), and to investigate the instability of the ideal random alloys with respect to either phase separation or to the formation of some ordered phase. This can be performed using the generalized perturbation method (GPM) where the interaction parameters for an Ising-like description are derived by expanding the electronic energy about the random state treated in the CPA [1], or using the mean-field concentration functional (MF-CF) theory [8] based on an adaptation of the classical density functional theory of fluids to a lattice gas model of binary alloys. The advantage of both the GPM and the MF-CF approaches is that they allow one to account for the concentration dependence of the effective interatomic interactions. Both approaches encounter difficulties when applied to strongly interacting alloys; both are single-site theories neglecting the effect of fluctuations in the local environment and possible lattice distortions in the disordered phases.

Both groups of methods have so far been applied almost exclusively to alloy systems where all phases can be considered as either solid solutions or ordered superstructures on a single underlying simple lattice. Notable exceptions are the work of Fernández Guillermet *et al* [9] on phase stabilities in the Pt–W system (where both fcc and bcc solid-solution phases but no ordered intermetallic compounds have been considered), and the work of Lu *et al* [10] on alloys of Cu with Rh, Pd, Pt and Au and on the Ni–Al systems. Among these alloys, only CuAu has an fcc-based superstructure, while CuPt has the rhombohedral $L1_1$ structure and CuPd and NiAl crystallize in the bcc B2 structure. The cluster expansion has been extended to the calculation of the enthalpies of formation of these alloys, but only for Ni–Al has an attempt been made to compute finite-temperature thermodynamic properties on the basis of a simplified cluster expansion and has the Ni-rich half of the phase diagram been calculated. The challenge evidently is to treat systems where phases based on more than one basic lattice coexist with complex lattices that can be derived from neither of these elementary structures.

In the present paper we report on an attempt to construct the phase diagram of such a complex alloy system from first principles. The Pd–V system has been chosen for our investigations because

(i) due to the difference in occupation of the d band, Pd–V is a strongly interacting system, having a relatively large energy of formation with an asymmetric dependence on composition,

(ii) the crystal structures of the two elements are different; hence both fcc and bcc solid solutions must be considered,
(iii) the phase diagram shows at least one phase (PdV_3 with the A15 structure) that cannot be considered as a superstructure of the elemental lattices.

Hence the phase diagram is complex, but not so complex as to make the attempt at a full *ab initio* calculation hopeless. We try to take full advantage of recent progress in *ab initio* total-energy calculations:

(i) We consider a reasonably large number of candidates for the structures of the ordered phases and perform a full structural optimization for all of these lattices. This certainly leads to an improved accuracy of the predicted structural energy differences compared to that of calculations neglecting differences in the volumes of formation and the relaxation of the internal structural degrees of freedom.
(ii) Disordered alloys are modelled by large supercells containing 32 atoms, using different randomly generated atomic configurations at least at some compositions. This adds to the averaging over the 32 different lattice sites present already in a single model. For each model, a full structural relaxation is performed, i.e. we account both for the fluctuations in the local environment and for local atomic displacements from the ideal lattice. On the other hand, we deliberately take a simple approach in the statistical-mechanical part of the problem: we use a mean-field approximation with Bragg–Williams order parameters to describe the effect of long-range ordering in those cases where the ordered superstructures have energies lower than those of the random alloys, and Warren–Cowley order parameters in the opposite case where short-range ordering is expected to dominate. For both models the interaction parameters are derived from a fit to the calculated total energies. The solid-state part of the complete Pd–V phase diagram has been calculated and the success seems to confirm the strategy that we have adopted.

In addition, we present a detailed analysis of the electronic spectra of both ordered intermetallic compounds and solid solutions.

2. Methodology

Ground-state energies and electronic structures of ordered intermetallic compounds and of disordered alloys in the palladium–vanadium system have been calculated using the Vienna *Ab initio* Simulation Package [11–14] based on local density functional theory. Disordered alloys are represented by random atomic configurations in large 32-atom supercells with an overall face-centred-cubic (fcc) or body-centred-cubic (bcc) structure (section 2.1). The effect of long-range ordering (LRO) is described in the framework of Bragg–Williams theory [15] (section 2.2). To consider short-range ordering (SRO) we use Warren–Cowley SRO parameters [16] with a quadratic correction to the configurational entropy as proposed by Tsatskis [17] (section 2.3). The interchange energy determining the energy and entropy of mixing as a function of the LRO parameters, as well as the pair interactions determining the energetics associated with SRO, are derived from the total energies of the supercells.

2.1. LDF calculations

VASP solves the Kohn–Sham equations of LDF theory in a plane-wave basis set. The electronic ground state is determined via an iterative unconstrained band-by-band matrix-diagonalization scheme based on a residual-minimization method (RMM) [14,18]. To calculate the new charge density and potential after each iteration, an improved Pulay mixing is implemented [19]. To

account for the nonlocality in the exchange–correlation functional we used the generalized gradient approximation (GGA) as proposed by Perdew and Wang (PW91) [20]. Brillouin-zone integration is performed with Monkhorst–Pack grids [21] using a generalized Gaussian smearing [22] for structural relaxations and the tetrahedron method with Blöchl corrections [23] for the calculation of densities of states. All results have been checked for convergence with respect to the number of k-points. The respective grid chosen for each of the calculations depends on the number of atoms in the supercell; typical grids will be given in the sections below. An energy cut-off of 250 eV is used throughout all calculations.

The electron–ion interaction is described by the projector augmented-wave (PAW) method of Blöchl [24], as further improved by Kresse and Joubert [25]. In the PAW approach the exact shape of the valence wavefunction is taken into account, which improves the description of transition metals. The 3p states of vanadium are treated as valence states to guarantee a good transferability of the potential.

The optimization of the atomic geometry is performed in two ways, depending on the type of the unit cell. For cells having just one degree of freedom (cubic cells with atoms on high-symmetry positions), the minimum of the energy versus the volume is found by fitting several calculations at different volumes to a Murnaghan equation of state [26]. For all other cells a quasi-Newtonian algorithm is used to relax cell size and shape as well as the positions of atoms not on high-symmetry positions.

2.2. Long-range order

The main focus of our work is on the electronic and ground-state properties of the intermetallic compounds and disordered alloys. Therefore only simple statistical approaches are used for describing the effect of long- and short-range atomic ordering on the energetics of the disordered alloys and for the construction of the phase diagram. To find the stable phase at a given temperature and atomic concentration of the constituents, the free enthalpy or Gibbs free energy ΔG of formation $\Delta G = \Delta H - T\,\Delta S$ has to be determined for all competing phases by minimization of ΔG with respect to all structural degrees of freedom. Only the configurational entropy has been considered in describing ΔS; all vibrational contributions to the free energy of formation have been neglected. For completely disordered two-component mixtures the configurational entropy is given by the ideal entropy of mixing. Ordering reduces the configurational entropy. We describe long-range order on a given superlattice (fcc or bcc) using the Bragg–Williams LRO parameter [15]

$$\eta = \frac{f_\alpha - x_\mathrm{A}}{1 - x_\mathrm{A}}. \tag{1}$$

Here f_α is the fraction of α-sites occupied by atoms of type A and x_A is the concentration of A atoms. In the case of complete order, A and B atoms sit only on α- and β-sites of the superlattice, respectively; therefore $\eta_\mathrm{ord} = 1$. Complete disorder is described by $\eta_\mathrm{dis} = 0$. By defining f_β as the fraction of β-sites occupied by A atoms, it is calculated to be

$$f_\beta = x_\mathrm{A} - \frac{c_\mathrm{A}}{c_\mathrm{B}} x_\mathrm{B} \eta$$

with $c_{\mathrm{A,B}}$ denoting the fractions of α- and β-sites, respectively. The configurational entropy in the case of long-range order is then given by

$$\Delta S_\mathrm{LRO} = -Nk\{c_\mathrm{A}[f_\alpha \ln f_\alpha + (1 - f_\alpha)\ln(1 - f_\alpha)] + c_\mathrm{B}[f_\beta \ln f_\beta + (1 - f_\beta)\ln(1 - f_\beta)]\}. \tag{2}$$

The variation of the energy of formation with the degree of LRO depends on the interatomic interactions. Considering nearest-neighbour interactions only, the energy of formation for a

completely disordered alloy is given by $\Delta E(\eta = 0) = Nzx_A x_B W_{AB}$ where z is the coordination number and the interchange energy W_{AB} is defined by $W_{AB} = \frac{1}{2}(V_{AA} + V_{BB}) - V_{AB}$ with V_{IJ} being the pair interaction in an IJ pair. Within the Bragg–Williams mean-field approximation, LRO provides an additional contribution of $\Delta E(\eta) = zW_{AB}\eta^2/4$ to the energy of formation. The degree of LRO in equilibrium is determined by minimizing ΔG with respect to η.

The interchange energy is determined from our total-energy calculations for the pure metals and supercells of disordered alloys. V_{AA} and V_{BB} are calculated from the cohesive energies of the pure metals, V_{AB} and W_{AB} can then be calculated for every given disordered configuration. For the Pd-rich alloys the resulting interchange energies show an almost perfectly linear increase with increasing V concentration; for details see below.

2.3. Short-range order

Short-range order is described by the Warren–Cowley SRO parameters [16, 27] defined by

$$\alpha_{ij} = 1 - \frac{\langle p_i^A p_j^B \rangle}{x_A x_B} \tag{3}$$

where p_i^A and p_j^B are the probabilities of finding an atom of type A on position i and one of type B on position j, respectively. The degree of order α_n in the nth shell around a given atom is found by averaging over all atoms in this shell. The α_n can have positive as well as negative values with $-1 \leqslant \alpha_{n,\min} \leqslant \alpha_n \leqslant \alpha_{n,\max} \leqslant 1$. $\alpha_i = 0$ corresponds to complete disorder. $|\alpha_{n,\min}|$ and $|\alpha_{n,\max}|$ depend on the lattice and the concentrations of the constituents of the alloy due to geometrical constraints [28, 29]. SRO leads in a second-order approximation to a quadratic correction of the LRO configurational entropy [17]:

$$\Delta S_{SRO} = \Delta S_{LRO} - Nk\frac{1}{4}\sum_n z_n \alpha_n^2 \tag{4}$$

where z_n is the coordination number for the nth shell. The energy of formation in the case of SRO is calculated via the shell interaction energy $V_n = \frac{1}{2}(V_{AA,n} + V_{BB_n}) - V_{AB,n}$ (here $V_{AA,n}$, $V_{BB,n}$ and $V_{AB,n}$ are the interaction energies for two atoms of the respective types which are nth-nearest neighbours):

$$\Delta E_{SRO} = Nx_A x_B \sum_n c_n V_n (1 - \alpha_n). \tag{5}$$

The equilibrium SRO is again found by minimizing ΔG with respect to all α_n (and η in the case of additional LRO), taking into account the geometrical constraints on the values of the α_n.

In our calculations we consider the interaction of atoms with two shells of nearest neighbours. The energy of formation and the SRO parameters α_n are known; hence the concentration-dependent shell interaction parameters may be extracted by inverting equation (5).

3. Structure and stability of ordered intermetallic compounds

The fundamental problem in theoretical investigations of the phase stability of binary alloys is the lack of a general algorithm for creating candidate structures. Many observed ordered structures of intermetallic compounds are based on superstructures of the simple fcc, bcc and hcp structures. If certain restrictive assumptions on the nature of the interactions between the atoms are made, the possible structures may be enumerated. Exact results are available for the cases of nearest- and second-nearest-neighbour interactions only; see for example the review of Ducastelle [1]. However, this is not sufficient to account for all existing structures, and it is known that to yield some observed structures further interactions have

to be considered [3, 30, 31]. An analysis of fcc superstructures in palladium–vanadium alloys has been performed by Wolverton and co-workers [6, 7, 32]. However, this approach excludes structures based on entirely different crystal lattices.

A more empirical approach in the search for candidate structures is to investigate the 'chemical vicinity' of Pd–V as given by the Pettifor structure maps [33, 34]. Structures realized for chemically similar alloys are expected to represent realistic candidate structures. Figure 1 shows the Pettifor tables for all stoichiometries that are not empty around Pd–V. In the following we discuss each stoichiometry separately.

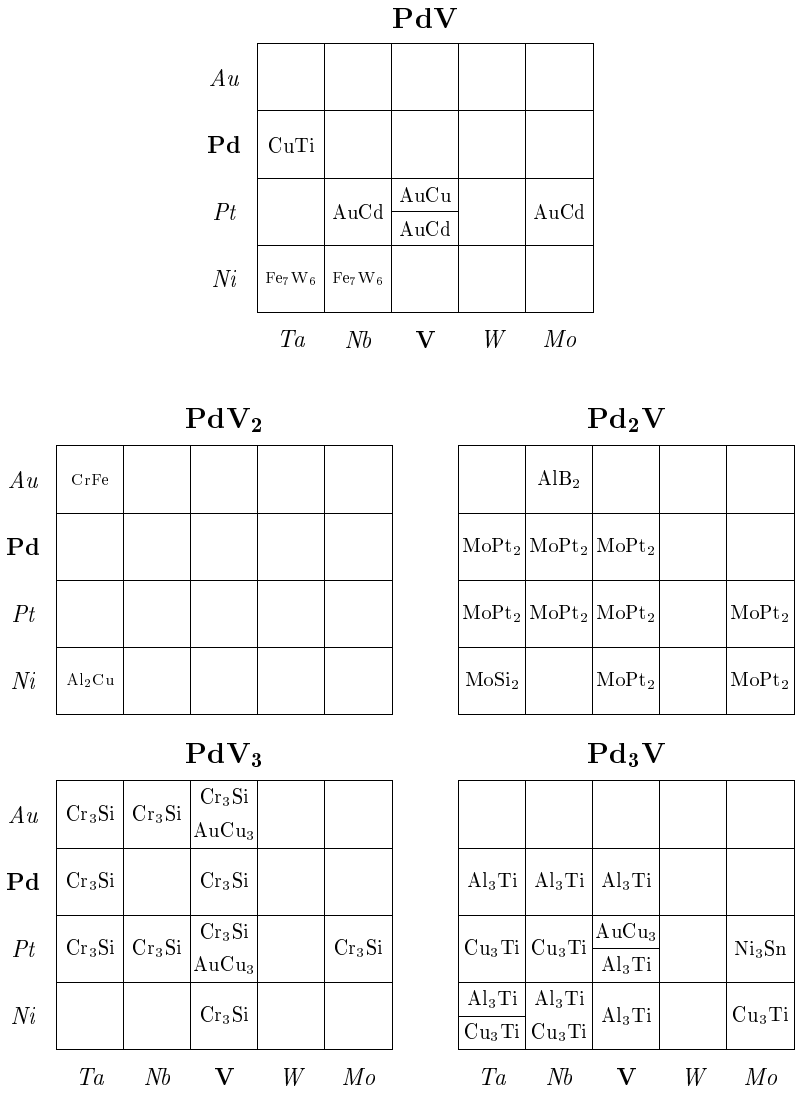

Figure 1. Pettifor tables for different stoichiometric alloys in the 'chemical vicinity' of the palladium–vanadium alloys. The labels name the prototypes of the stable structures found experimentally. Multiple entries denote that more than one structure was found for a compound. Two structures separated by a horizontal line indicate the identification of a low-temperature (bottom) and a high-temperature (top) phase.

3.1. Pd_3V

The ordered superstructures for A_3B alloys stabilized by nearest- and next-nearest-neighbour interactions are the Al_3Ti ($D0_{22}$), $AuCu_3$ ($L1_2$) and Al_3Zn ($D0_{23}$) structures based on an fcc lattice, the Cu_3Ti ($D0_a$) and Ni_3Sn ($D0_{19}$) structures based on an hcp lattice and the $AlFe_3$ ($D0_3$) structure based on the bcc lattice [1]. As can be seen in figure 1, all but $D0_3$ and $D0_{23}$ are realized in the chemical vicinity of Pd_3V, although the $AuCu_3$ structure occurs only as a high-temperature phase of Pt_3V. Polymorphism is also reported for Ni_3Ta and Ni_3Nb, which crystallize in the Al_3Ti as well as the Cu_3Ti structure. In the case of Ni_3Ta the two structures were identified as high- and low-temperature phases, respectively. Therefore these four structures are investigated as possible structural variants of Pd_3V.

The four structures are very similar. All of them are superstructures of close-packed lattices and the twelve nearest neighbours of every vanadium atom are palladium atoms. The cubic $AuCu_3$ ($L1_2$) and the hexagonal Ni_3Sn ($D0_{19}$) structures are based on different stacking variants of close-packed layers with A_3B stoichiometry within each layer, ABC stacking leading to cubic and AB stacking to hexagonal symmetry. In both structures A has twelve B neighbours, while B has eight B and four A neighbours. In the $L1_2$ structures all atomic positions are fixed by symmetry; in the $D0_{19}$ structure the axial ratio is a free parameter. Similarly the Al_3Ti ($D0_{22}$) and Cu_3Ti ($D0_a$) structures may be considered as different stacking variants of the same basic structure (cf. figure 2). In fact the two structures can easily be transformed into each other by shifting the atoms of every second hcp (Cu_3Ti) layer in the z-direction from its hcp to its neighbouring fcc hollow and vice versa. For the Al_3Ti structure this leads to a unit cell composed of two tetragonally distorted $AuCu_3$ cells with a step-shift at the interface. In terms of the stacking of the close-packed layers, this leads to a long-period stacking sequence, but the constraint of tetragonal symmetry reduces the variable structural parameters to the axial ratio. In the Cu_3Ti structure the stacking of the close-packed layers is AB, but the distortion of the hexagonal layers reduces the symmetry to orthorhombic such that there are six variable structural parameters (b/a, c/a and four internal positional parameters; cf. table 1). The Al_3Zn ($D0_{23}$) structure can be considered as consisting of alternating $L1_2$ and $D0_{22}$ lattices. The nearest-neighbour coordination is the same in all five structures; the complete avoidance of direct neighbours of the minority atoms appears to be one of the determining structural principles.

Table 1. Positions of the atoms in the energetically most stable Pd_3V and Pd_2V ordered phases at $T = 0$ K. Our *ab initio* results are compared to experimental values where available.

		Experiment				Theory		
Atom	Position	x	y	z	Reference	x	y	z
Cu_3Ti								
V	2a	—				0	0	0.659
Pd1	2b	—				0	1/2	0.347
Pd2	4f	—				0.249	0	0.166
$MoPt_2$								
V	2a	0	0	0	[59]	0	0	0
Pd	4g	0	0.340	0		0	0.339	0

Typical k-point grids for the calculation of the ground-state energy in unit cells consisting of eight atoms with aspect ratios close to unity are $8 \times 8 \times 8$. The optimized lattice constants of all structures are compiled in table 2, together with the experimental values of the stable structures. Table 2 and figure 3 present also the calculated energies of formation.

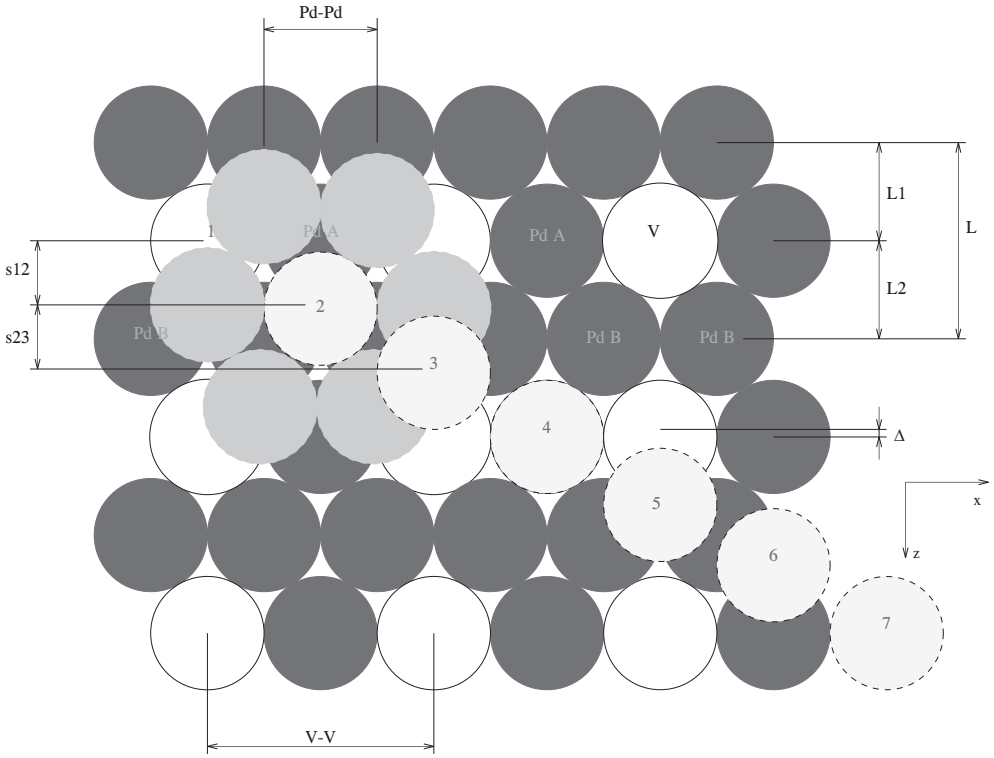

Figure 2. Stacking sequences for the Al_3Ti ($D0_{22}$) and Cu_3Ti ($D0_a$) structures: vanadium atoms in subsequent layers are on positions $1234567\cdots$ and $12121\cdots$, respectively. $D0_{22}$ consists of two slightly elongated fcc cells (aspect ratio $a/c = 1.014$); the atoms are placed on high-symmetry positions which leaves only one free parameter (a/c) that changes some of the distances indicated. The $D0_a$ structure has a slightly distorted hcp stacking and the atoms are not on high-symmetry positions. The six free parameters (b/a, c/a, z(PdA), z(PdB), z(V), x(PdB)) influence all distances indicated in the plot.

The $D0_{19}$ and $L1_2$ structures are clearly energetically disfavoured. Although the difference in atomic volume is small, this appears to be sufficient to disfavour these highly symmetric structures with no internal degrees of freedom (only the hexagonal axial ratio may be adjusted in the $D0_{19}$ structure). Both the $D0_{22}$ and $D0_a$ structures have additional internal degrees of freedom whose relaxation allows one to lower the energy. Experimentally, $D0_{22}$ was found to be the stable phase of Pd_3V, but our calculations show the $D0_a$ phase to lie about 6 meV/atom below $D0_{22}$. Again this has to be attributed to the greater flexibility of the $D0_a$ structure: while the atoms in the $D0_{22}$ structure are placed on high-symmetry positions, which reduces the number of free parameters (at fixed volume) to one, this is not the case for Cu_3Ti. Three free z-coordinates and one free x-coordinate in addition to the axial ratios raise the number of free parameters in this structure to six, and thereby allow all distances indicated in figure 2 to adjust for the minimal energy. On freezing the atoms in the $D0_a$ lattice at their hcp high-symmetry positions, the energy difference between Al_3Ti and Cu_3Ti vanishes.

The apparent discrepancy between theory and experiment can also be explained by the fact that while experiments are always carried out at finite temperatures, our calculations are performed at $T = 0$ K. For the chemically similar binary alloy Ni_3Ta, experiment has found a low-temperature Cu_3Ti phase besides the high-temperature $D0_{22}$ crystal [35, 36]. Hence our

Table 2. Lattice parameters, total energies and energies of formation ΔE of ordered Pd–V alloys. The types of the intermetallic compounds are labelled by their prototype structure and the Structure Report designation where available. Measured lattice parameters for alloys found experimentally are noted. ΔH_M is the enthalpy of formation calculated using the Miedema model [45]. Distances are given in Å, energies in electron volts per atom.

	Structure		Lattice parameters					
Alloy	Prototype	Struct. Report symbol	Experiment	Theory	E	ΔE	ΔH_M	%Pd
Pd	Cu	A1	$a = 3.88$	$a = 3.956$	−5.206			100
Pd_3V	Ni_3Sn	$D0_{19}$	—	$a = 5.422$ $c = 4.416$	−6.285	−0.151	−0.332	75
Pd_3V	$AuCu_3$	$L1_2$	—	$a = 3.902$	−6.317	−0.183	−0.332	75
Pd_3V	Al_3Ti	$D0_{22}$	$a = 3.847$ $c = 7.753$	$a = 3.869$ $c = 7.848$	−6.380	−0.246	−0.332	75
Pd_3V	Cu_3Ti	$D0_a$	—	$a = 5.469$ $b = 4.467$ $c = 4.808$	−6.386	−0.252	−0.332	75
Pd_2V	$MoSi_2$	$C11_b$	—	$a = 3.214$ $c = 8.449$	−6.648	−0.205	−0.435	67
Pd_2V	$MoPt_2$		$\bar{a} = 2.745$ $\bar{b} = 8.240$ $\bar{c} = 3.740$	$a = 2.790$ $b = 8.321$ $c = 3.720$	−6.712	−0.269	−0.435	67
PdV	CsCl	B2	—	$a = 3.095$	−6.965	0.097	−0.549	50
PdV	NaTl	B32	—	$a = 3.068$	−7.109	−0.048	−0.549	50
PdV	AuCd	B19	—	$a = 4.348$ $b = 2.712$ $c = 4.811$	−7.224	−0.162	−0.549	50
PdV	CuTi	B11	—	$a = 3.048$ $c = 6.152$	−7.246	−0.184	−0.549	50
PdV	AuCu	$L1_0$	—	$a = 3.790$ $c = 3.917$	−7.249	−0.187	−0.549	50
PdV_2	$MoSi_2$	$C11_b$	—	$a = 3.095$ $c = 9.152$	−7.658	−0.022	−0.477	33
PdV_3	$AlFe_3$	$D0_3$	—	$a = 3.025$	−8.001	−0.012	−0.373	25
PdV_3	Cr_3Si	A15	$a = 4.828$	$a = 4.816$	−8.117	−0.127	−0.373	25
V	W	A2	$a = 3.03$	$a = 2.994$	−8.917			0

calculations indicate the possibility of a similar low-temperature phase transition in Pd_3V.

A number of total-energy calculations for Pd_3V compounds have been published in the literature [5, 7, 37–39], concentrating on the structural energy difference between the $L1_2$ and $D0_{22}$ structures. Using linearized muffin-tin-orbital (LMTO) calculations in the atomic-sphere approximation (ASA), Garbulsky and Ceder [5] find $\Delta E = 68$ meV/atom, Wolverton and Zunger [7] find $\Delta E = 66.8$ meV/atom using the same technique and $\Delta E = 71.5$ meV/atom using the linearized augmented-plane-wave (LAPW) method, Lebacq *et al* [39] find $\Delta E = 69.3$ meV/atom using a full-potential LMTO approach. All calculations

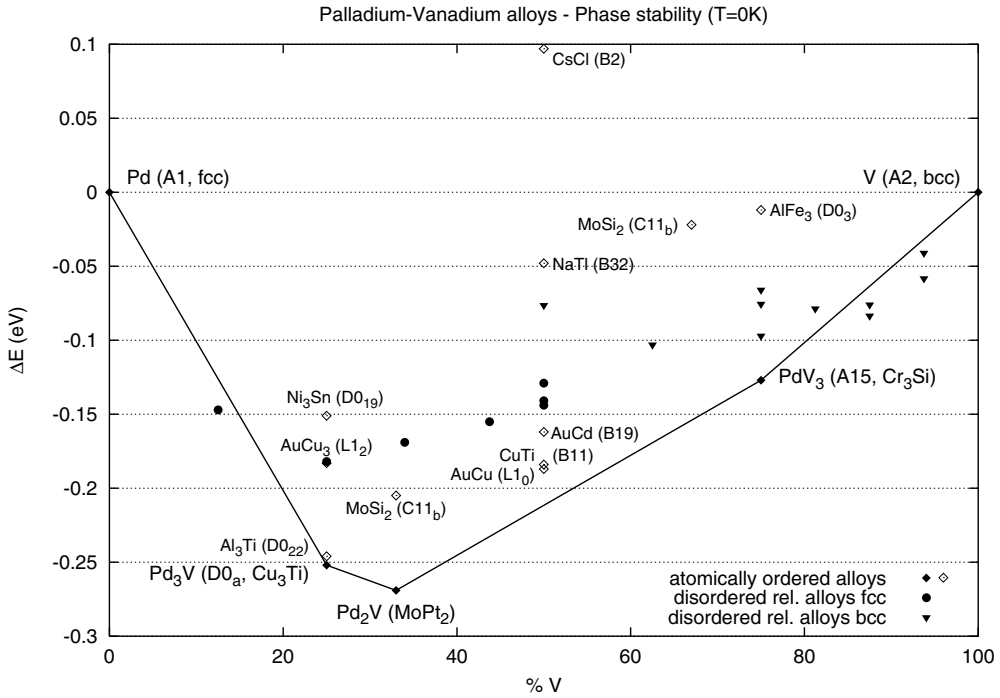

Figure 3. Formation energies of ordered and disordered palladium–vanadium alloys. The labels give the prototype structure and the reported structure designation where available. The line indicates the phase stability of ordered alloys.

have been performed for the experimental crystal structures. Hence the small difference compared to our result of $\Delta E = 63$ meV/atom is to be attributed to the lack of full structural relaxation in the earlier calculations. The Cu_3Ti structure was not considered in the earlier DFT calculations. Wolverton and Zunger [38] have also pointed out that the high density of states of $L1_2$-type Pd_3V leads to a magnetic instability of the paramagnetic phase which reduces the structural energy difference to about 39 meV/atom. They have also argued that due to the high DOS at E_F, electron–hole excitations are energetically more favourable in the $L1_2$ than in the $D0_{22}$ structure and that this could explain why the dominant wavevector of the experimentally observed high-temperature SRO phase is not coincident with that of the LRO phase [40]. We shall come back to this point below.

3.2. Pd_2V

For the compound richest in Pd, all candidate structures are characterized by the absence of V–V neighbours. For vanadium concentrations larger than 25% it is no longer possible to avoid V–V nearest-neighbour pairs in superstructures based on the fcc lattice. Among the possible ordered superstructures listed by Ducastelle [1], only the $MoPt_2$ structure has been observed experimentally. The $MoPt_2$ structure can be regarded as a superstructure of the fcc lattice with a minimum of Mo–Mo and a maximum of Mo–Pt bonds: Mo has only two Mo and ten Pt nearest neighbours; Pt has five Mo and seven Pt neighbours. As figure 1 shows, binary compounds chemically similar to Pd_2V mainly crystallize in this structure. Only for Ni_2Ta and Au_2Nb were the $MoSi_2$ ($C11_b$) and AlB_2 (C32) structures, respectively, reported. The

$C11_b$ ($MoSi_2$) structure is very similar to the $MoPt_2$ phase, but is based on a tetragonal unit cell as opposed to an orthorhombic cell for $MoPt_2$. Nearest-neighbour bonds of the minority atoms are avoided for aspect ratios $c/a < 3\sqrt{2} = 4.42$. For $c/a = 3$ the atoms are on the sites of a bcc lattice. There are two more ideal axial ratios: for $c/a = 3\sqrt{2}/\sqrt{3} = 2.38$, close-packed layers with 2:1 stoichiometry are stacked in a bcc AB packing (the atoms in layer B lie on bridge sites of layer A), whereas at $c/a = 3\sqrt{2} = 4.42$ a close-packed arrangement is achieved. The $C11_b$ structure can be stabilized only by long-range interactions beyond second neighbours [1]. The C32 structure is based on a hexagonal lattice. For axial ratios of $c/a = \sqrt{6} = 2.45$ and $c/a = \sqrt{3}/\sqrt{8} = 0.612$ it can easily be distorted to an fcc and bcc phase, respectively. Nevertheless, in the true C32 phase the B–B distance is always less than the Al–B distance, which in the case of Pd_2V would contradict the assertion of an energetical advantage of Pd–V bonds at this stoichiometry.

All three structures have been calculated with a k-point mesh of $9 \times 9 \times 9$. The AlB_2 phase yields a positive energy of mixing and is therefore discarded. Of the two other structures, the $MoPt_2$ phase turns out to be the more stable one, in agreement with experiment, with a structural energy difference of 269 meV per atom. When the structure is set up in an orthorhombic cell the axial ratio of the two shorter sides is $a/c = 0.75$, close to the value of $1/\sqrt{2} = 0.71$ for a perfect fcc lattice. The experimental lattice parameters in table 2 are means of two sets of published results [41, 42].

3.3. PdV

Ordered intermetallic compounds of the PdV type are of special interest for us, since the experimental phase diagram [42,43] shows a solid-solution $Pd_{50}V_{50}$ fcc phase down to at least 600 K. However, Maldonado and Schubert [44] reported the observation of cubic superlattice reflections for a 50 at.% alloy after holding it for 12 hours at 600 °C.

The possible fcc superstructures stabilized by short-range interactions are CuAu ($L1_0$), CuPt ($L1_1$) as well as two further structures (listed as AB and A_2B_2) which have not been observed in alloys. The hexagonal superstructures are AuCd (B19) and a further structure that has not yet been observed. The ordered bcc structures are the CsCl (B2), NaTl (B32) and CuTi (B11) types. The Pettifor tables (figure 1) suggest CuTi (B11), AuCd (B19) and AuCu ($L1_0$) as possible structures. Fe_7W_6 ($D8_5$) was reported for NiTa and NiNb, but is not a stoichiometric AB compound. At equiatomic composition it can be formed only at a high concentration of antisite defects and was therefore not considered.

The AuCu ($L1_0$) and AuCd (B19) structures can be described in terms of stacking alternate rectangular layers of A and B atoms parallel to (100) such that close-packed layers with 1:1 stoichiometry are obtained. Provided that the axial ratio of the tetragonal cell does not deviate too much from the ideal value unity, ABC stacking of the close-packed layers is achieved in the AuCu structure. In structures with smaller axial ratios, an intermediate state between a close-packed structure and bcc 110 layers in bcc stacking is realized, the transformation to bcc being complete at $c/a = 0.707$. An AB stacking sequence is realized in the AuCd (B19) structure, but the bond angles within the layers are closer to those in bcc 110 layers than in close-packed layers. In the ideal AuCu structure each atom has eight unlike and four like neighbours; the same coordination is realized in the ideal AuCd lattice. In the CuPt ($L1_1$) structure the atoms are arranged in alternate close-packed layers with a long-period repeat sequence ABCA′B′C′, leading to a complex rhombohedral cell. In the B2 structure perfect heterocoordination is realized on the bcc lattice (each atom has eight unlike nearest and six like second-nearest neighbours), whereas in the B32 structure each atom has four like and four unlike neighbours. The CuTi (B11) structure may be regarded as an ordered arrangement

of the bcc structure in which pairs of ordered layers of the two components alternate along the (001) direction, the tetragonal cell consisting of two bcc cells. For $c/a = 2$ and equal interlayer spacings (ideal bcc configuration), each atom has four like and four unlike nearest neighbours. Our calculated aspect ratio of $c/a = 2.02$ lies close to that value. A reduced axial ratio and displacements of the layers along (001) lead to an increase of the number of unlike neighbours from four to five.

All calculations have been performed using $9 \times 9 \times 9$ k-points; the results are again compiled in table 2 and figure 3. The common structures based on a basic bcc lattice are all energetically unfavourable; for the B2 structure the energy of formation is even endothermic and for the B32 structure it is only weakly exothermic. The B11 structure on the other hand has an energy of formation that is only 2% smaller than that of the most favourable AuCu ($L1_0$) structure; the B19 structure lies more than 10% above them. The fact that the B2 structure is energetically so extremely unfavourable suggests that heterocoordination is no longer a dominant factor in the chemical bonding. In the two energetically most favourable structures, short V–V bonds are formed: within the bilayers of the B11 structure vanadium atoms come as close as 2.60 Å. The shortest distances within the pure V layers in the $L1_0$ structures are 2.68 Å. This indicates that at this concentration, the formation of V–V bonds is becoming energetically favourable. In this connection it is worth mentioning that an arrangement of V atoms along chains occurs also in the A15 (Cr_3Si) PdV_3 phase (see below).

Altogether however we find that, as figure 3 shows, all atomically ordered PdV phases lie energetically well above the mixture of Pd_2V with PdV_3, which rules out another stable phase at 50 at.% V and $T = 0$ K.

3.4. PdV_2

The Pettifor tables show no ordered phases of composition 1:2 in the chemical environment of PdV_2. To test the energetics of ordered phases related to the bcc structure of pure V, we have considered the $MoSi_2$ ($C11_b$) structure (cf. section 3.2). Ordered fcc superstructures (Ga_2Zr at this composition) in the V-rich regime have been investigated by Kohan *et al* [6] and found to be energetically unfavourable. They were therefore not considered in the present study.

The optimized axial ratio for $C11_b$-type PdV_2 is $c/a = 2.96$; i.e. only a small deviation from an ideal bcc crystal is predicted. The calculated energy of formation is only very weakly exothermic ($\Delta E = 22$ meV/atom), and this is insufficient to stabilize the structure against the competing Pd_2V and PdV_3 phases.

3.5. PdV_3

In this V-rich regime, the bcc packing of V is expected to be dominant: $AlFe_3$ ($D0_3$) is an ordered superstructure of the bcc lattice but is not reported for any compound similar to PdV_3. The Pettifor tables (see figure 1) show that many binary alloys similar to PdV_3 crystallize in a Cr_3Si (A15) phase. V chains located at the faces of the cubic cell stretch along all three main axes through a Pd bcc lattice. The A15 structure cannot be regarded as derived from any of the elementary metallic structures. The other structure proposed by the Pettifor table is $AuCu_3$ ($L1_2$) which is a superstructure of the fcc lattice.

Again $9 \times 9 \times 9$ k-points were used to determine the ground-state energy. The results are summarized in table 2. For the $L1_2$ structure we calculate an endothermic energy of formation; the formation of the $D0_3$ structure is only very weakly exothermic; the A15 structure is clearly the energetically most favourable one, in agreement with experiments.

3.6. Summary—intermetallic compounds

Collecting all of our results together, we have found the stable Pd–V alloy series consisting of the prototype structures Pd (fcc)–Pd_3V (Cu_3Ti)–Pd_2V ($MoPt_2$)–PdV_3 (Cr_3Si)–V (bcc). Except for the Cu_3Ti phase, which is just another stacking of the Al_3Ti structure, this is in agreement with the experimental findings. We suspect that the Cu_3Ti phase could be the low-temperature phase of Pd_3V.

The calculated lattice constants of the compounds agree with experiment within the bounds set by the errors in the calculated lattice constants of the pure elements (Pd: $\Delta a = +2\%$—here the GGA corrections to the LDA value overshoot somewhat, which is characteristic for the heavier elements—and V: $\Delta a = -1.1\%$—here the LDA error is larger and the GGA leads to better agreement with experiment). Calculated axial ratios and the values of the internal coordinates are in excellent agreement with experiment. Unfortunately no experimental values for the energies of formation are available. In table 2 we list for comparison the values calculated using the Miedema model [45]. Quite generally, the Miedema values are larger than our results, especially in the V-rich range. That the Miedema values are much too large is also confirmed by the available experimental results for the homologous Pt–V system where the model predictions are too large by a factor of up to two. The model also predicts a different concentration dependence of the heat of formation ΔE, which is larger in the V-rich regime, in disagreement with our results. We shall come back to this point when we discuss the phase diagram.

The energies of formation can also be extracted from the earlier DFT calculations. However, as these investigations were concerned primarily with order–disorder transitions on a basic fcc lattice, the energies of formation are given relative to a hypothetical fcc phase of V. If we adopt this convention, we find that our energies of formation ($\Delta E = -309, -352, -312$ meV/atom for Pd_3V, Pd_2V and PdV in the stable crystal structures) are consistently less exothermic than the results obtained by Wolverton and Zunger (WZ) [7] and Garbulsky and Ceder (GC) [5] using the LMTO-ASA ($\Delta E = -348, -393, -367$ meV/atom (WZ), $-350, -394, -365$ meV/atom (GC)). The A15-type PdV_3 compound has been considered only by Kohan *et al* [6]; using LMTO-ASA, an energy of formation of $\Delta E = -450$ meV/atom (relative to fcc V) was reported. This figure is considerably more exothermic than our result of -315 meV/atom.

The differences in the calculated energies of formation are to be attributed to the use of generalized gradient corrections in our calculations, whereas previous calculations used the local density approximation. We note that the GGA leads to improved cohesive energies and lattice parameters for the pure metals [46, 47]; the present work demonstrates that it also leads to improved predictions for the heats of formation of binary alloys.

4. Electronic structure of ordered intermetallic compounds

Despite the thorough investigation of the Pd–V alloy system, experimental results on the electronic structure of such compounds are very rare. Nemnonov *et al* have performed SXS measurements on binary alloys of vanadium with late transition elements [48, 49], including the Pd–V system [50], reporting V Kβ_5 and Pd L_{III} spectra at various compositions. The V Kβ_5 spectrum arises from transitions out of the V 4p states. At larger Pd contents, the K spectrum develops a two-peak structure with the subband at higher binding energy, attributed to a hybridization with the 4d states of Pd. This is confirmed by comparing its position with respect to the Fermi level with the peak in the Pd L_{III} spectrum reflecting the intensity distribution in the Pd 5s4d bands. For PdV_3, in addition V M_{II-III} spectra measuring the 3p3d

states have been reported. The peak in the M spectrum coincides with the low-energy peak of the K spectrum. Altogether the SXS spectra have been interpreted as evidence of a splitting of about 2.5 to 3 eV between the d-band maxima of the two components, showing little variation with composition. However, the resolution of the SXS spectra is rather modest and the structure of the alloys has not been characterized. It remains unclear whether the experiments have been performed on ordered compounds or on disordered alloys.

More recent experimental investigations on the electronic properties of ordered Pd–V alloys have been mostly electronic specific heat measurements [51–53], for which the experimental information is restricted to the immediate vicinity of the Fermi level. For all stable Pd–V compounds except the A15-type PdV_3 phase, a relatively low DOS at E_F with only a weak concentration dependence has been reported. The DOS of the disordered phases is substantially higher and it has been concluded that the ordered superstructures are stabilized by the formation of a pseudogap which appears as a result of ordering. The DOS is only slightly higher for the A15-type compound, but in this case, disordering leads to a small decrease of the DOS. *Ab initio* investigations of the electronic spectrum have been presented for the competing $D0_{22}$ and $L1_2$ phases of Pd_3V [38, 39]. The electronic structure of the A15 (Cr_3Si) phase for transition metal alloys in general has been treated by Turchi *et al* [54].

The general trends in the electronic spectra of alloys of a late and an early transition metal have been discussed by Hausleitner and Hafner [55] as functions of the difference in number of d electrons, the chemical composition and the degree of structural ordering. The most important feature is the formation of a complex of strongly hybridized d bands. For alloys with a large difference in d-band filling such as Pd–V, the d-band complex has a bimodal character, with the lower part of the band dominated by the orbitals of the late transition metal (here Pd) and the upper part overlapping with the Fermi level dominated by the states of the early transition metal. Within each band the bond order for the dominating species changes sign about in the middle of the d band. The depth of the pseudogap separating the subbands increases with the degree of atomic ordering; at complete disorder it can disappear almost completely.

Figure 4 shows the density of states per atom for all stable ordered phases of the Pd–V alloy series as well as for the metastable AuCu phase. Full lines refer to mean values for all atoms, dashed and dotted lines to mean values for V and Pd atoms, respectively. The numbers in the plots give the centres of mass of the respective d bands in eV with respect to the Fermi energy.

We find that all Pd–V compounds except PdV_3 conform rather well with the simple qualitative picture sketched above. At the composition Pd_3V, the Fermi level falls very close to the DOS minimum separating the two subbands. In such a situation, both bonding and antibonding Pd subbands are almost completely filled; Pd–Pd binding is weak. The V subband is almost empty; hence again V–V binding is weak and the dominant chemical interactions occur between unlike atoms. With increasing V content, more bonding states in the V subband become occupied; hence the V–V interactions are strengthened. In the $MoPt_2$-type Pd_2V compound, the DOS minimum is rather broad, but it is clearly apparent that the Fermi level begins to move into the V-dominated band. In PdV the two subbands have about equal weight and the Fermi level falls at the centre of the V subband; the pseudogap has moved to higher binding energies. With increasing V content, the centre of gravity of the Pd d band is shifted to higher binding energies, by about 0.6 eV on going from Pd_3V to PdV, whereas the centre of the V d band remains almost stationary.

Figure 5 shows the DOSs for the $L1_2$, $D0_{22}$ and $D0_a$ structures of Pd_3V: in the $L1_2$ structure, the DOS shows a very sharp peak precisely at the Fermi level—our findings agree with those of previous investigations explaining the higher stability of the $D0_{22}$ structure with respect to $L1_2$ on the basis of the fact that in the former the Fermi level is shifted into the pseudogap [39]. The

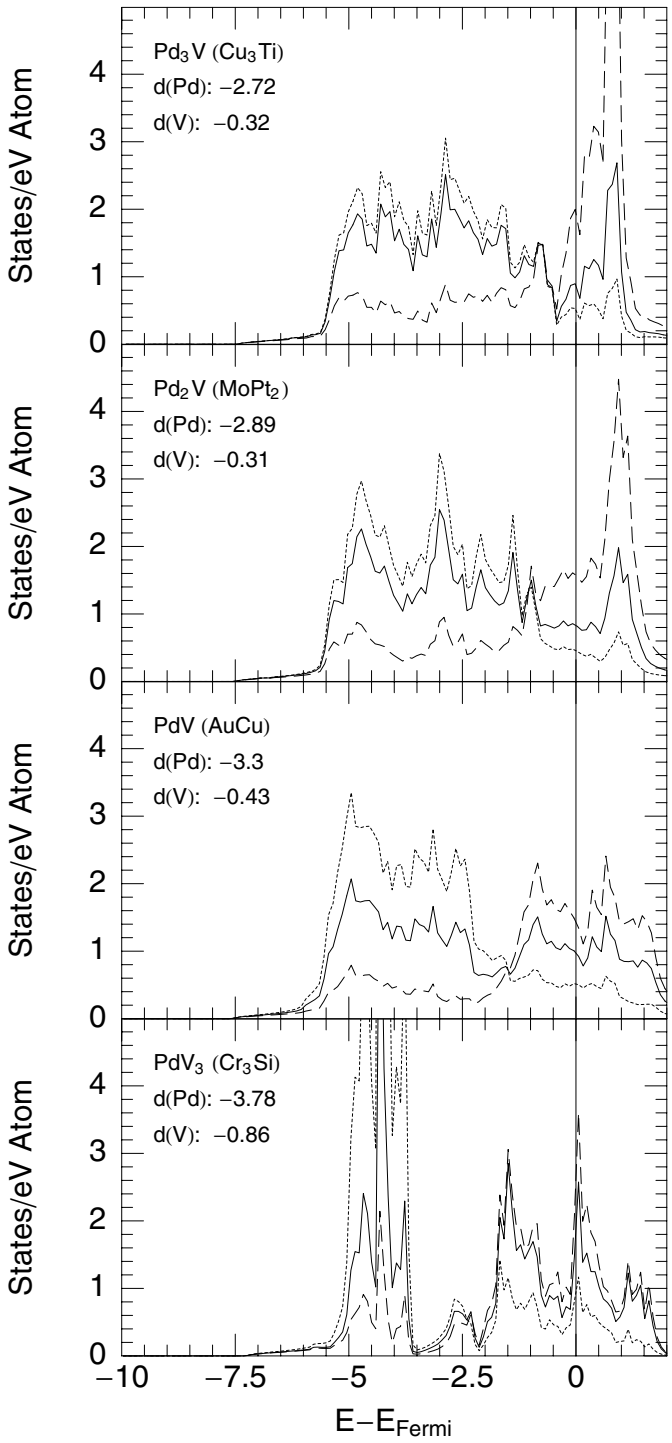

Figure 4. Total and local densities of states for ordered palladium–vanadium alloys. Full lines refer to the total DOS per atom, dotted and dashed lines to the average DOSs of palladium and vanadium atoms, respectively. The numbers in the keys indicate the centres of mass of the corresponding d bands in eV with respect to the Fermi level.

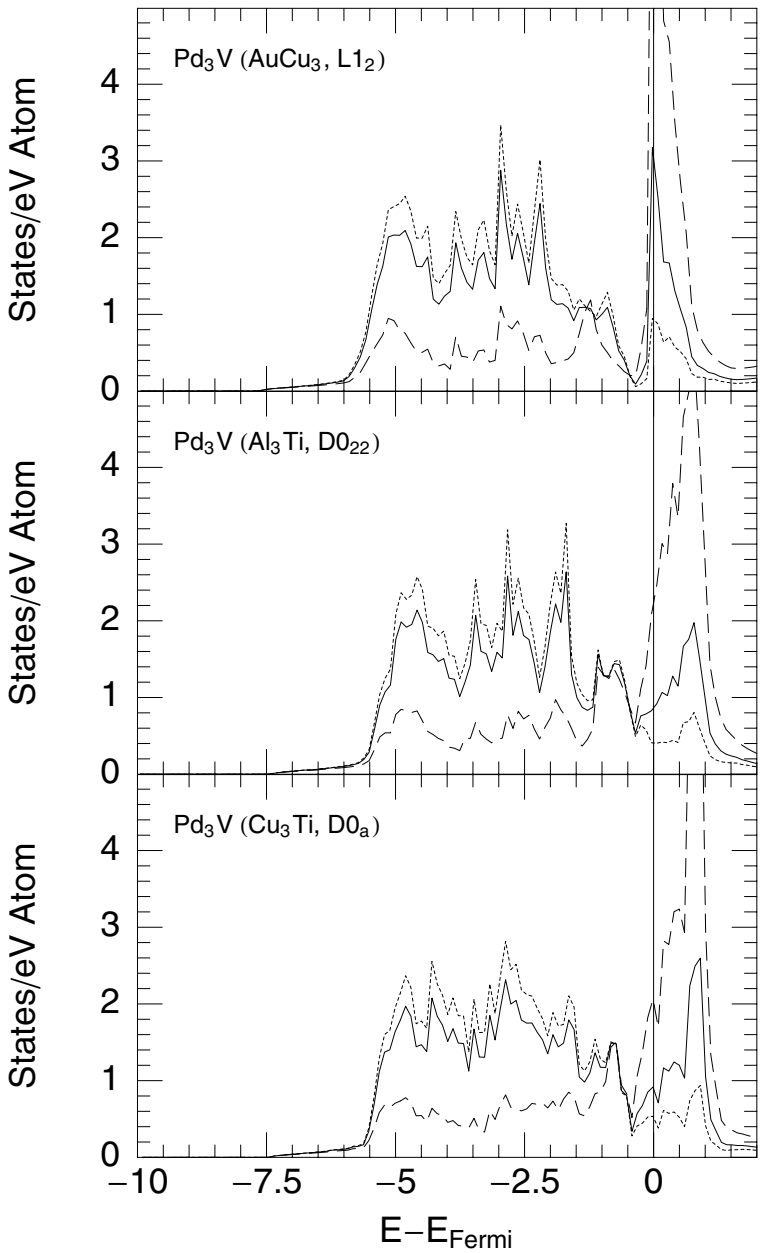

Figure 5. Total and local densities of states for differently ordered Pd_3V phases ($L1_2$, $D0_{22}$ and $D0_a$ from top to bottom). Dotted and dashed lines show the average DOSs of palladium and vanadium atoms, respectively.

DOSs of the structurally related Cu_3Ti and Al_3Ti phases are very similar; the higher structural complexity of the former leads to reduction of the peak heights in the DOS, but the structural energy difference is much too small to give rise to pronounced differences in the electronic spectrum. The high DOS at E_F of the $L1_2$ phase leads to a magnetic instability according to the Stoner–Wohlfarth criterion, but no spin-polarized calculations have been performed.

The electronic DOS of the A15-type PdV_3 compound differs significantly from that of any other alloy in this system. The characteristic feature of this structure is quasi-one-dimensional chains of V atoms extending along all three coordinate directions and coupling only weakly with the Pd sublattice. In the electronic structure this is reflected by a clear separation of the d bands; the positions of their centres of mass differ by 2.8 eV, in quite good agreement with the experimental value of 2.6 eV found by the SXS studies by Nemnonov *et al* [48]. The position of the Fermi level close to a sharp peak in the DOS is characteristic for many alloys with the A15 structure [54].

5. Solid solutions

In most previous studies of order–disorder transitions and phase diagrams, the energetics of the disordered phases has been calculated from concentration-independent effective cluster interactions derived from total-energy calculations on a large number of disordered compounds. Here we adopt a different strategy. Ground-state energies and electronic densities of states for disordered solid solutions are calculated for supercells representing disordered solid solutions of the minority atoms in the host lattice (fcc on the Pd-rich and bcc on the V-rich side of the phase diagram). In both cases the supercells consist of 32 atoms. The distributions of the two species over the lattice positions within the supercell are created using a random-number generator; the lattice parameter of the supercell as well as the positions of all of the atoms are allowed to fully relax.

5.1. V in fcc Pd

Disordered fcc Pd–V phases are investigated in a supercell built of $2 \times 2 \times 2$ fcc unit cells containing 32 atoms. A k-point mesh of $3 \times 3 \times 3$ is used during the optimization of the atomic geometry using a conjugate gradient technique; the grid is refined to $5 \times 5 \times 5$ for the calculation of the DOS. Calculations are carried out for several vanadium concentrations ranging from 12.5 at.% to 50 at.%. The configurations are checked for their randomness by requiring the number of nearest neighbours of the two types to be approximately normally distributed around the mean value ($x_{\mathrm{Pd}}z$ and $x_{\mathrm{V}}z$ Pd and V neighbours, respectively, around each atom, z being the coordination number).

The mixing energies ΔE per atom are compiled in figure 3. From the values for 50 at.% where we have created a number of different configurations, the rms fluctuations of the energy of formation as a function of the atomic configuration can be estimated to be about ± 10 meV per atom. The gain in the energy of formation from the relaxation of the atomic positions is between 15 and 40 meV/atom; the atoms are shifted by 0.03 to 0.2 Å from their high-symmetry positions. Bond lengths in the relaxed structure vary between 2.6 and 2.9 Å; the Pd–Pd and V–V distances in the clean crystals are 2.8 and 2.6 Å, respectively. The energy gain from relaxation does not depend systematically on the concentrations of the constituents.

One can immediately see that for low V concentrations up to about 15 at.%, solid solutions are preferred already at $T = 0$ K over a mixture of pure Pd and the ordered Pd_3V alloy. At higher V contents, the energies for disordered solutions lie well above those for the ordered fcc structures (and even above that for the bcc $C11_b$ structure at 33 at.% V), which explains the tendency to long-range order and a preference for heteroatomic bonds. At 50 at.% the energetically most favourable random configuration has an energy of formation that is 80 meV/atom lower than that of the ordered phase. This makes the stability of a fcc solid solution at 400 °C as indicated by the experimental phase diagram rather unlikely.

5.2. Pd in bcc V

The bcc supercells in the vanadium-rich part of the phase diagram consist of $4 \times 2 \times 2$ bcc unit cells with 32 atoms; grids of $2 \times 4 \times 4$ and $3 \times 6 \times 6$ k-points are used for the relaxation and the DOS calculation, respectively. Palladium concentrations range from 12.5 at.% to 50 at.%.

The mixing energies per atom are again plotted in figure 3. The variance of the energy values at a single concentration is slightly higher than on the fcc side, since due to the less dense bcc lattice, larger relaxation effects occur in our comparatively small supercell. Although the atoms do not shift further than about 0.2 Å from their high-symmetry positions (comparable to the shift in fcc solid solutions), the energy gain from relaxation is as high as 70 meV/atom in the $Pd_{50}V_{50}$ alloy. However, for bcc disordered structures the relaxation effects depend on the atomic concentrations. In $Pd_{6.5}V_{93.5}$ compounds, atoms only move up to 0.1 Å from their high-symmetry positions, yielding a gain in the energy of formation of only 15–20 meV/atom. Bond lengths in the relaxed crystals vary between 2.5 and 2.8 Å; although most of the shortest bonds are of V–V type, no definite preference for V–V bonds can be observed (also a few Pd–V and Pd–Pd bonds are as short as 2.5 Å).

Again, at low concentration, solid solutions are energetically preferred over a mixture of pure V and the ordered A15 phase. The solid solutions were compared with ordered structures on the bcc lattice (CsCl, NaTl, $MoSi_2$, $AlFe_3$). All of them have formation energies lower than those of the disordered phases; hence long-range ordering on a bcc lattice with a preference for heterocoordination is energetically unfavourable. However, ordered intermetallic compounds such as the CuTi (B11) phase derived from the bcc lattice or completely new structures such as A15 can be substantially lower in energy than the disordered bcc solid solutions, indicating a tendency to short-range ordering with some preference for direct V–V bonds.

6. Electronic structure of solid solutions

Figures 6(a) and 6(b) show the DOSs of disordered solutions on the fcc and bcc lattices. On comparing them to the DOSs of the ordered phases (figure 4), one observes the disappearance of the pseudogap separating the d bands of the two components. The electronic spectra are also different from those of the pure metals; in particular the large bonding–antibonding splitting characteristic for the bcc transitions metals does not appear in the DOSs of the bcc solid solutions. At approximately equiatomic composition, the DOS is essentially rectangular as assumed in the Friedel model; at higher concentrations of one species, the DOS is canted to the side of the majority atoms as assumed in Pettifor's model [56] for the electronic structure of transition metal alloys. The increased $n(E_F)$ compared to that of ordered intermetallic compounds for palladium-rich alloys accounts for the experimentally observed increase of the paramagnetic susceptibility χ and the electronic specific heat coefficient γ [52].

When considering the partial DOSs around V and Pd atoms individually, the separation of the bands can still be clearly recognized. The Pd d-band centre of mass is shifted towards higher binding energies with increasing V concentrations through the whole series of calculated phases, i.e. also across the fcc–bcc phase boundary. While the position of the vanadium d-band centre of mass also changes by about 0.35 eV for fcc solids, it remains fairly constant on the bcc side. The energy interval between Pd and V d-band centres of mass is highest for $Pd_{12.5}V_{87.5}$ (bcc). Compared to those for the ordered phases, the d bands are located at lower binding energies, i.e. closer to the Fermi energy, and the energy interval from Pd to V is lower in solid solutions. This result confirms that the lower energy of mixing for disordered solutions is also indicated by the DOS.

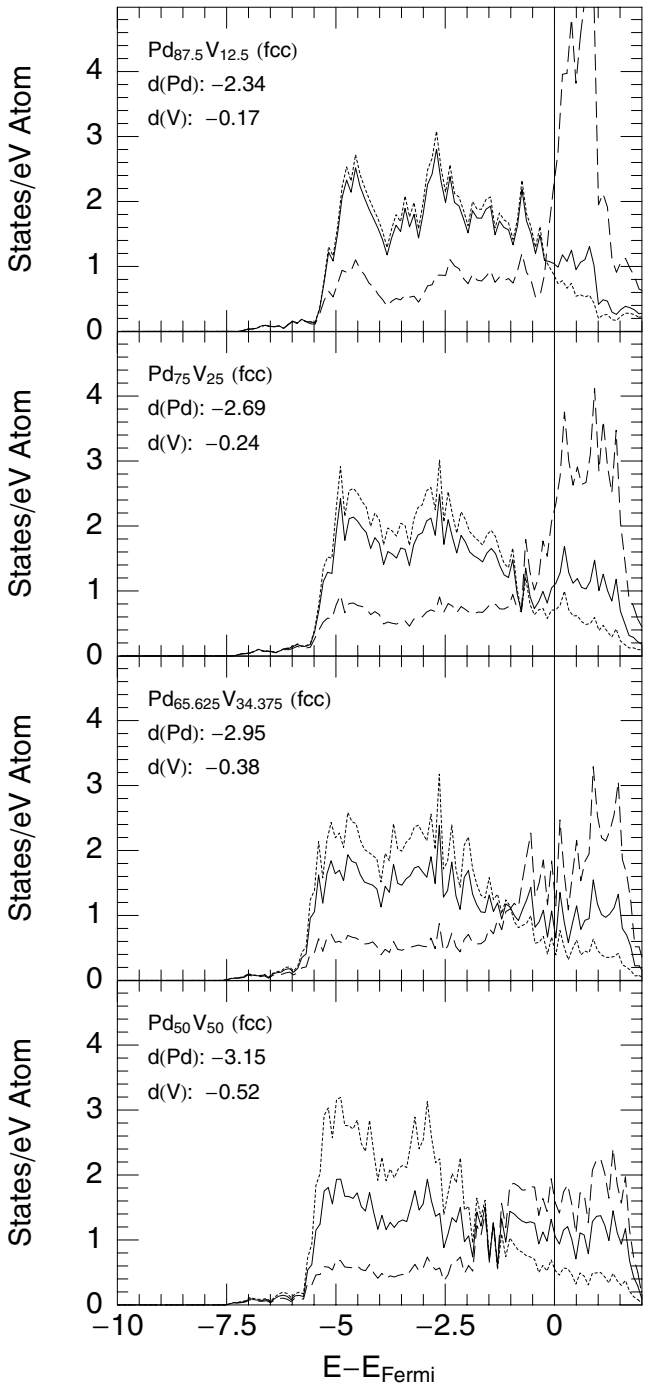

Figure 6. Total and local densities of states for disordered palladium–vanadium alloys on fcc (a) and bcc (b) lattices. Full, dotted and dashed lines refer to the total DOS and the average DOSs of palladium and vanadium atoms, respectively. The numbers indicate the centres of mass of the d bands in eV relative to E_F. (a) The DOS for random fcc Pd–V alloys. The calculated supercells have 32 atoms, among which there are 28, 24, 21 and 16 Pd atoms from top to bottom, respectively. (b) The DOS for random bcc Pd–V alloys. The 32-atom large supercells contain 16, 12, 8 and 4 Pd atoms from top to bottom.

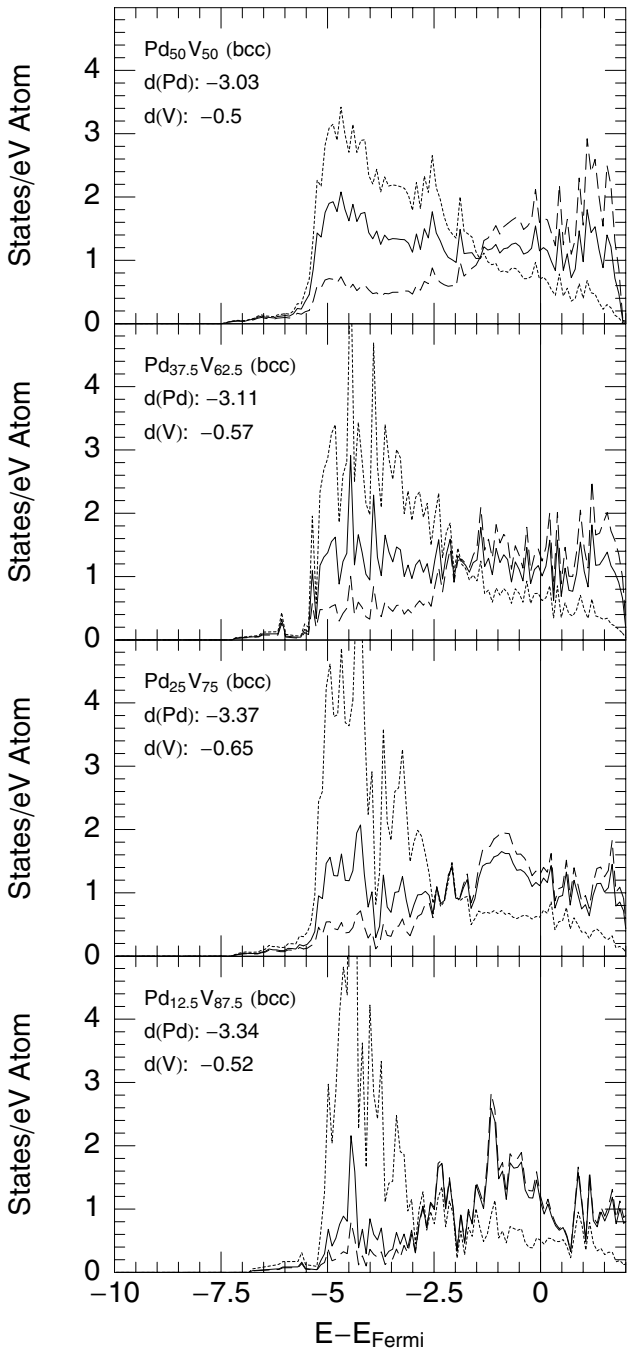

Figure 6. (Continued)

7. Temperature-dependent ordering

In order to construct the alloy phase diagram, the most favourable temperature-dependent structure has to be found for every concentration and temperature. The internal energies of all

systems have been calculated with very high accuracy. On the other hand, we deliberately make an attempt to use only the simplest statistical methods for calculating the entropic contributions to the finite-temperature thermodynamic properties and for the determination of the phase diagram. The justification for this procedure is its success. However, when comparing with standard approaches based on cluster expansions, one should note that the pair interactions derived from our data are effective potentials incorporating the effects of both a global relaxation of the density and a local relaxation of all atomic degrees of freedom. As discussed in the previous sections, the energy change induced by a local relaxation can be considerable. Hence our approach also offers some advantages compared to standard cluster expansion, where local relaxations are usually neglected.

As noted above, Pd–V alloys strive for long-range order (heterocoordination) in Pd-rich phases but exhibit only short-range order when the majority of atoms are vanadium. The main formulae used were introduced at the beginning of the paper.

7.1. Long-range order in fcc alloys

The first step for the LRO regime of the phase diagram is to determine the concentration-dependent nearest-neighbour interchange energy defined as $W_{\mathrm{AB}} = \frac{1}{2}(V_{\mathrm{AA}} + V_{\mathrm{BB}}) - V_{\mathrm{AB}}$, with V_{IJ} being the nearest-neighbour pair interactions. W_{AB} is always negative for compounds that do not segregate. The energy of mixing for a given configuration can also be expressed in terms of the V_{IJ} when the relative number of nearest neighbours of specific types is known. V_{AA} and V_{BB} can be extracted from the pure bulk energies; altogether this yields V_{AB} and W_{AB} for every calculated disordered configuration (cf. figure 7).

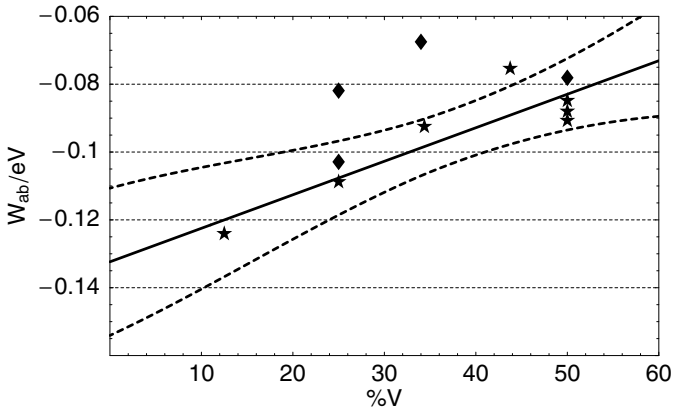

Figure 7. A linear fit of the interchange energy W_{AB} to the energy of formation of selected configurations for solid solutions (stars); the double-sided 95% confidence interval is marked by the dashed lines. The rhombi represent the interchange energies calculated for the ordered intermetallic compounds.

A least-squares fit shows that a W_{AB} depending linearly on composition is a reasonable first approximation. Since we are searching for the lower bound of the energies of mixing of disordered solutions we take the lower bound of the 95% confidence interval of a linear fit to the calculated values for the W_{AB} to determine the energy of mixing of solid solutions at $T = 0$ K.

Around the stoichiometry of energetically preferred long-range-ordered alloys on fcc superlattices, partially ordered phases form at 0 K. Their free energy of formation is determined by applying the Bragg–Williams mean-field approximation; the optimal long-range-order

parameter is given by the variational condition. It turns out that due to the relatively small difference in energy of mixing of ordered and disordered phases, the concentration range of preferred ordered structures is already very small at $T = 0$ K (about ± 2 at.% from the stoichiometric ratio). The critical temperatures may be determined by comparing the free energies of the partially ordered intermetallic compounds and of the disordered solid solutions and by calculating the temperature dependence of the order parameter from the variational condition. If the two values agree, a second-order phase transition is predicted; otherwise the transition is first order. For Pd–V, a second-order transition is found for the Au–Cu-type PdV compound (which, however, is only metastable compared to a $Pd_2V + PdV_3$ mixture; see below), whereas the order–disorder transitions in $MoPt_2$-type Pd_2V and Al_3Ti-type Pd_3V are predicted to be first order, as confirmed by the analysis of the free energy in the vicinity of T_c (see figure 8). This is a consequence of the distortions from the ideal structures observed in these phases. However, we have to emphasize that these distortions have been calculated only by a static optimization of the structure—a consideration of temperature-dependent lattice distortions would require a full *ab initio* MD simulation. The critical temperatures T_D for the order–disorder phase transitions are at 1059 K, 1183 K and 727 K for the Al_3Ti, $MoPt_2$ and AuCu fcc superstructures respectively.

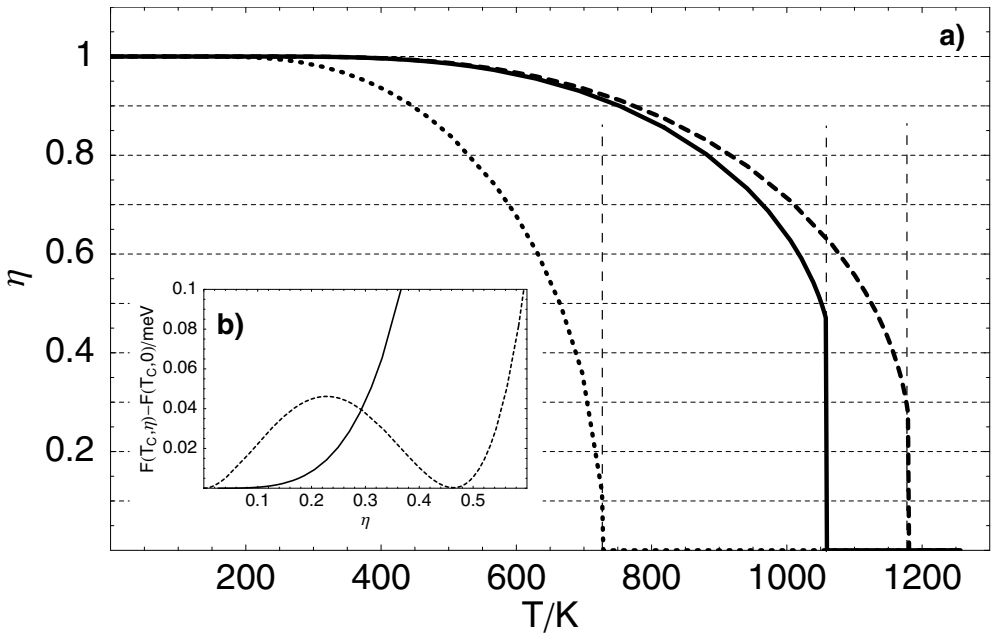

Figure 8. (a) Temperature-dependent long-range-order parameters for the fcc-based Pd–V superstructures: dotted line—PdV (AuCu); dashed line—Pd_2V ($MoPt_2$); full line—Pd_3V (Al_3Ti). The vertical lines mark the critical temperatures calculated by equating the free energies of the competing phases. (b) The difference in free energy of the partially ordered phase ($\eta > 0$) versus the disordered fcc solid solution ($\eta = 0$) for $L1_0$-type PdV showing a second-order transition (full line) and for $D0_{22}$-type Pd_3V showing a first-order phase transition (dashed line); cf. the text.

7.2. Short-range order in bcc alloys

In the case of short-range order, it is not just the first-nearest-neighbour shell interaction energy that needs to be considered. The energy of mixing for disordered bcc solutions is obtained

by setting $\alpha_n = 0$ in equation (5), with V_n standing for the interaction energy of atoms that are nth-nearest neighbours. For the calculated configurations, all values in equation (5) but the shell interaction energies are known. In our case, two linearly concentration-dependent shell interaction energies (V_1 and V_2) are fitted to the resulting set of equations; the V_i ($i \geqslant 3$) are assumed to be zero. The fitted interaction energies yield for given short-range parameters $\alpha_i \neq 0$ ($i = 1, 2$) mixing energies within ± 10 meV of the simulated values. The quality of the fit does not improve on including up to four shell interaction energy values.

For Pd concentrations up to far beyond reasonable values for bcc disordered phases the nearest-neighbour shell interaction energy V_1 is positive while V_2 is negative (cf. figure 9), indicating the preference for nearest neighbours of the same atom type, but second-nearest neighbours of different types in bcc alloys. The mixing energy of the CsCl structure of +0.1 eV/atom impressively confirms this result. However, the energetically most favourable SRO parameters of $\alpha_1 = 1$ and $\alpha_2 = -1$ are topologically not achievable. For a $Pd_{50}V_{50}$ alloy the long-range-ordered structure that exhibits the most favourable short-range order is the NaTl phase. Indeed, as figure 3 shows, this structure has a mixing energy of 150 meV/atom below CsCl and is one of the few stable long-range-ordered bcc phases.

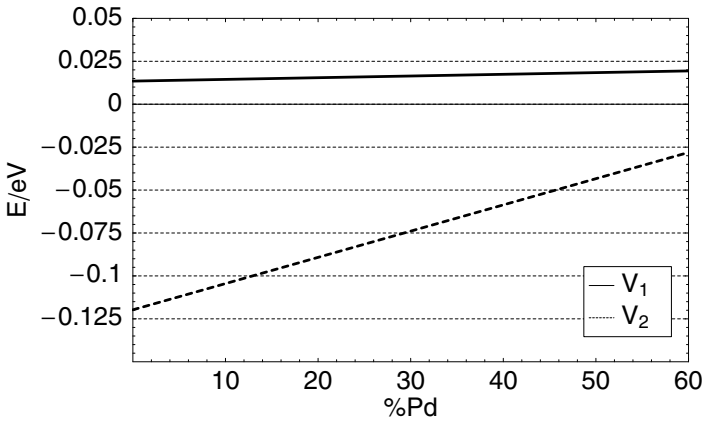

Figure 9. Concentration-dependent shell interaction energies V_1 and V_2 for bcc-based Pd–V superstructures.

The configurational entropy is obtained according to equation (4) by adding a quadratic correction term to the ideal mixing entropy. Minimizing the free energy with respect to all α_n yields for the optimal SRO parameters

$$\alpha_n = \frac{2x_A x_B V_n(x)}{kT} \qquad (n = 1, 2). \tag{6}$$

For low temperatures the so-determined values for the $|\alpha_n|$ are outside the geometrically allowed region for the bcc lattice. In this temperature range, which is below 500 K for a Pd concentration up to 40 at.% but rises sharply beyond that concentration, the energetically most favourable short-range-ordered configuration lies on the border of the allowed α-field.

Including only quadratic corrections to the entropy (equation (4)) might result in unphysical negative values for S_{SRO} in the case of large $|\alpha_n|$. However, in our calculations this is only the case at low temperatures above 40 at.% Pd. Here the energy difference between short-range-ordered bcc alloys and the mixture of ordered phases is already very large (cf. figure 3). A hypothetical order–disorder phase transition lies far above 2000 K, so the inappropriate approximation for S_{SRO} has no effect on the resulting phase diagram. In cases where this

temperature–concentration range could not be neglected, corrections beyond second order for the entropy need to be introduced by extending the approach described in reference [17].

8. Phase diagram construction

Now that we have calculated the free energies for the series of stable intermetallic compounds as well as the temperature- and concentration-dependent free energies of formation of substitutional fcc alloys with a certain degree of long-range order and of substitutional bcc alloys with short-range order, the Pd–V alloy phase diagram can be constructed using the method of double tangents. The resulting phase diagram (see figure 10) is in very good agreement with the experimental one [42], especially on the Pd-rich side.

The temperatures for the Pd_3V and Pd_2V order–disorder phase transitions as well as for the eutectoid transition of Pd_3V + Pd_2V to the fcc solid solution agree within $\pm 4\%$. The concentration of the eutectoid transition is, at 26.5 at.% V, only 5% below the experimental value.

On the vanadium-rich side of the phase diagram the disagreement is larger. The dashed lines in figure 6 show parts of the metastable phase diagram. The theoretically determined peritectoid phase transition at 75 at.% V is 300 K too low with a $Pd_2V + \alpha$ two-phase region for about 100 K between the experimentally observed phases. The reason for this disagreement is either a heat of formation for the A15 phase that is too low (by about 25 meV/atom $\widehat{=}$ 300 K) compared to that of the V-rich compounds, or our neglect of the vibrational contributions to the entropy. If the phonons in the A15-type PdV_3 compound are softer than those in the fcc-based Pd-rich compounds, the larger vibrational entropy could stabilize the A15 phase to higher temperatures.

The neglect of the vibrational entropy is probably also responsible for the miscibility gap at high temperatures having too large a width. Concentrated solid solutions tend to have more low-frequency modes than dilute random alloys, leading to a lowering of the free energy.

A remarkable point in the theoretical phase diagram is the lack of an fcc solid solution at low temperature at compositions slightly below 50 at.% V. We find a eutectoid minimum at 657 °C and 45 at.% V. Given the energetics derived from the DFT calculations, we see no possibility of reconciling theory and this particular detail of the phase diagram: the total energy of a fcc solid solution close to a 50/50 composition is definitely above that of all fcc compounds considered in this study, and these energies are in turn above that of a $Pd_2V + \alpha$ two-phase mixture. More exothermic heats of formation of the V-rich phases would make the low-temperature stability of a 50/50 disordered fcc alloy even more precarious. In this connection the observation of superlattice reflections for annealed 50/50 alloys is relevant [44]. However, the structural information is not sufficiently well described to provide a clue to a possible crystal structure. In any case, even the existence of a possible ordered low-temperature PdV phase could hardly explain the existence of an—even partially ordered—solid-solution phase at this composition. The experimental phase diagram in this concentration range certainly deserves re-examination.

9. Discussion and conclusions

We have presented detailed *ab initio* density functional studies of the atomic structure, energetics and electronic properties of crystalline intermetallic compounds and of substitutional alloys (treated in a supercell approximation) in the Pd–V system. All crystal structures have been fully relaxed. The *ab initio* calculations lead to structural results in full agreement

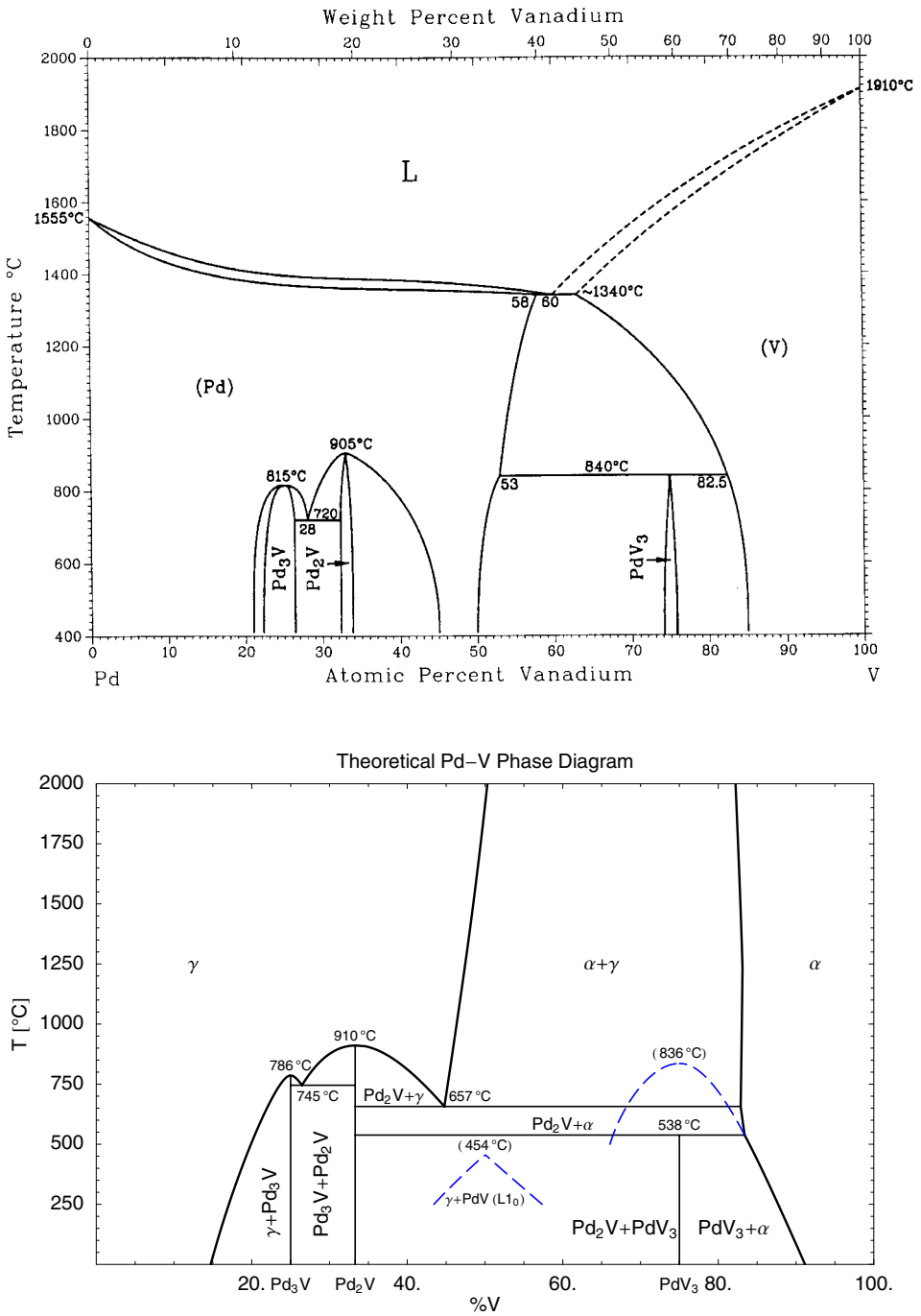

Figure 10. Experimental [58] (top) and theoretically determined (bottom) palladium–vanadium alloy phase diagrams. The dashed lines in the lower panel are parts of the metastable phase diagram.

with experiment—except for Pd_3V where a low-temperature phase transition to a Cu_3Ti-type structure is predicted. Given the existence of stable intermetallic compounds with this structure

in the immediate 'chemical vicinity' of Pd–V, this result does not seem to be unreasonable and merits experimental verification.

The energies of formation calculated for various random configurations of fcc and bcc solutions are used to deduce the interchange energy W_{AB} for fcc Pd-rich solid solutions and shell interaction energies V_n, $n = 1, 2$, for bcc V-rich solid solutions. The different treatment of fcc and bcc substitutional alloys is suggested by the fact that ordered fcc superstructures are always lower in energy than random fcc alloys, whereas the energetic ordering is inverted for the bcc phases.

Interchange energy and shell interactions have been used to calculate the free energy and the optimal degree of ordering of the intermetallic compounds using Bragg–Williams mean-field theory for the long-range-ordered fcc phases and Warren–Cowley short-range-order parameters and a second-order expansion of the configurational entropy for the bcc phases. While the energetics of the competing phases has been calculated very accurately—using a full-potential all-electron DFT method, gradient corrections to the exchange–correlation functional, full convergence with respect to the basis set, Brillouin-zone sampling etc—the statistical-mechanical approach to the free-energy calculation is admittedly—and deliberately—extremely simplified. This simplification is motivated by the fact that we intended to calculate the complete phase diagram and not only the coherent part based on a single basic crystal lattice.

Nevertheless, the calculated phase diagram is in good agreement with experiment—especially for the Pd-rich part. This is a rather remarkable result, given the modest agreement of the critical temperatures for order–disorder transitions obtained on the basis of cluster-expansion calculations. On one hand, the better agreement reflects the improved energetics produced by the gradient-corrected DFT calculations and the importance of full lattice relaxations for predicting heats of formation for the solid solutions (remember that the effect can be as large as 70 meV/atom); on the other hand, it demonstrates that our simplified approach to the free-energy calculations is adequate. In this context it is worth emphasizing that we have treated not only a single order–disorder transition (here the good agreement could be largely fortuitous), but also a sequence of transitions at different compositions. Deviations between theory and experiment concerning the peritectoid decomposition of the A15-type PdV_3 phase and the width of the two-phase field separating the two terminal solid solutions at higher temperatures are to be attributed to our neglect of vibrational contributions to the entropy. The vibrational spectra of both ordered compounds and substitutional solid solutions can in principle be calculated by *ab initio* force-constant methods [57] and using *ab initio* molecular dynamics, but only at the cost of a very large computational effort.

A qualitative disagreement exists concerning the existence/nonexistence of an fcc solid solution at $\leqslant$50 at.% Pd and low temperatures. It is difficult to imagine changes in the calculated energetics that could result in the stability of a disordered 50/50 phase. An ordered compound, PdV, seems to be much more likely—in agreement with experimentally observed but unresolved superstructure reflections. In any case, this part of the phase diagram should be re-examined.

Our work shows that the energies of formation produced by DFT calculations are now sufficiently accurate to serve as the basis for *ab initio* phase diagram constructions. Further improvements in the statistical-mechanical part will undoubtedly be necessary, in particular as regards the vibrational contributions.

In addition, our study provides deeper insight into the electronic properties of Pd–V alloys. Each ordered intermetallic compound is characterized by a split-band electronic density of states, i.e. by a Pd-dominated band at higher binding energies separated by a pronounced DOS minimum from a V-dominated band around the Fermi level. With increasing V content the Pd

band is shifted to higher binding energies. The low values of the DOS at E_F are in agreement with electronic specific heat measurements; the d-band shift is in rough agreement with old soft-x-ray data, but evidently a closer inspection of the d-band structure by means of well-evolved photoelectron spectroscopy would be of great interest. Disordered solid solutions (both fcc and bcc) show DOSs of the common-band type which are very close to the rectangular-band model proposed by Friedel decades ago. Around a 50/50 composition of the alloy the band is symmetric; for a majority of one species, the DOS is skewed to the side of the majority atoms as proposed in Pettifor's band model used as the basis of his semi-empirical analysis of the heats of formation of d-band alloys. Again, the increase of the DOS at the Fermi level is in agreement with experiment, but a more detailed spectroscopic investigation seems to be desirable.

Acknowledgments

We gratefully acknowledge financial support by the Austrian Fonds zur Förderung der Wissenschaftlichen Forschung within the Science College 'Computational Materials Science' (FWF-WK004).

References

[1] Ducastelle F 1991 *Order and Phase Stability in Alloys (Cohesion and Structure vol 3)* (Amsterdam: Elsevier Science)
[2] de Fontaine D 1979 *Solid State Physics* vol 34 (New York: Academic) p 74
[3] Sanchez J M, Ducastelle F and Gratias D 1984 *Physica* A **128** 334
[4] Kanamori J and Kakehashi Y 1977 *J. Physique Coll.* **38** C7 274
[5] Garbulsky G D and Ceder G 1995 *Phys. Rev.* B **51** 67
[6] Kohan A F, Tepesch P D, Ceder G and Wolverton C 1998 *Comput. Mater. Sci.* **9** 389
[7] Wolverton C and Zunger A 1994 *Phys. Rev.* B **50** 10 548
[8] Stocks G M *et al* 1994 *Statics and Dynamics of Alloy Phase Transformations (NATO ASI Series B, vol 319)* ed P E A Turchi and A Gonis (New York: Plenum) p 305
[9] Fernández Guillermet A, Ozolinš V, Grimvall G and Körling M 1995 *Phys. Rev.* B **51** 10 364
[10] Lu Z W, Wei S H, Zunger A, Frota-Pessoa S and Ferreira L G 1991 *Phys. Rev.* B **44** 512
[11] Kresse G and Furthmüller J 1996 *Phys. Rev.* B **54** 11 169
[12] Kresse G and Hafner J 1994 *Phys. Rev.* B **49** 14 251
[13] Kresse G and Hafner J 1993 *Phys. Rev.* B **47** 558
[14] Kresse G and Furthmüller J 1996 *Comput. Mater. Sci.* **6** 15
[15] Bragg W L and Williams E J 1934 *Proc. R. Soc.* A **145** 699
[16] Cowley J M 1950 *Phys. Rev.* **77** 669
[17] Tsatskis I 1998 *J. Phys.: Condens. Matter* **10** 683
[18] Wood D M and Zunger A 1985 *J. Phys. A: Math. Gen.* **18** 1343
[19] Pulay P 1980 *Chem. Phys. Lett.* **73** 393
[20] Perdew J P and Wang Y 1992 *Phys. Rev.* B **45** 13 244
[21] Monkhorst H J and Pack J D 1976 *Phys. Rev.* B **13** 5188
[22] Methfessel M and Paxton A T 1989 *Phys. Rev.* B **40** 3616
[23] Blöchl P, Jepsen O and Andersen O K 1994 *Phys. Rev.* B **49** 16 223
[24] Blöchl P 1994 *Phys. Rev.* B **50** 17 953
[25] Kresse G and Joubert D 1999 *Phys. Rev.* B **59** 1758
[26] Kumar M 1995 *Physica* B **391** 212
[27] Cowley J M 1960 *Phys. Rev.* **120** 1648
[28] Buršík J and Weatherly G C 1999 *Phys. Status Solidi* a **176** 835
[29] Rempel A A and Gusev A I 1990 *Phys. Status Solidi* b **160** 389
[30] Asta M, Wolverton C, de Fontaine D and Dreyssé H 1991 *Phys. Rev.* B **44** 4907
[31] Wolverton C, Asta M, Dreyssé H and de Fontaine D 1991 *Phys. Rev.* B **44** 4914
[32] Wolverton C, Ceder G, de Fontaine D and Dreyssé H 1992 *Phys. Rev.* B **45** 13 105

[33] Pettifor D G 1984 *Solid State Commun.* **51** 31
[34] Pettifor D G 1986 *J. Phys. C: Solid State Phys.* **19** 285
[35] Nowotny H and Oesterreicher H 1964 *Monatsh. Chem.* **95** 982
[36] Ruhl R C, Giessen B C, Cohen M and Grant N J 1967 *J. Less-Common Met.* **13** 611
[37] Wolverton C, Zunger A and Lu Z W 1994 *Phys. Rev.* B **49** 16 058
[38] Wolverton C and Zunger A 1995 *Phys. Rev.* B **52** 8813
[39] Lebacq O *et al* 1998 *J. Alloys Compounds* **264** 31
[40] Solal F *et al* 1987 *Phys. Rev. Lett.* **58** 21
[41] Villars P and Calvert L 1991 *Pearson's Handbook of Crystallographic Data for Intermetallic Phases* vol 4 (Materials Park, OH: ASM International) p 4947
[42] Smith J F 1988 *J. Alloy Phase Diagrams* **4** 1
[43] Köster W and Haehl W-D 1958 *Z. Metallk.* **49** 647
[44] Maldonado A and Schubert K 1964 *Z. Metallk.* **55** 619
[45] de Boer B F *et al* 1988 *Cohesion in Metals: Transition Metal Alloys (Cohesion and Structure vol 1)* (Amsterdam: Elsevier Science)
[46] Ozolinš V and Körling M 1993 *Phys. Rev.* B **48** 18 304
[47] Philipsen P H T and Baerends E J 1996 *Phys. Rev.* B **54** 5326
[48] Nemnonov S A, Kurmaev E Z, Ishmukhametov B K and Belash V P 1971 *Phys. Status Solidi* b **46** 77
[49] Nemnonov S A *et al* 1972 *Bull. Acad. Sci. USSR—Phys. Ser.* **36** 291
[50] Kurmaev E Z, Belash V P, Nemnonov S A and Sorokina M F 1972 *Bull. Acad. Sci. USSR—Phys. Ser.* **36** 288
[51] Turek P and Kuentzler R 1981 *Physica* B+C **107** 257
[52] Turek P, Kuentzler R, Bieber A and Jesser R 1985 *Solid State Commun.* **53** 979
[53] Kuentzler R and Waterstrat R M 1986 *J. Less-Common Met.* **120** 317
[54] Turchi P, Treglia G and Ducastelle F 1983 *J. Phys. F: Met. Phys.* **13** 2543
[55] Hausleitner C and Hafner J 1992 *Phys. Rev.* B **45** 115
[56] Pettifor D G 1987 *Solid State Physics* vol 40 (New York: Academic) p 43
[57] Kresse G, Furthmüller J and Hafner J 1995 *Europhys. Lett.* **32** 729
[58] Massalski T B (ed) 1990 *Binary Alloy Phase Diagrams* (Materials Park, OH: ASM International)
[59] Giessen B C and Grant N J 1965 *J. Less-Common Met.* **8** 114